

Supplementary Material for
**“28 October 2022 (M_w 3.8) Goesan Earthquake Sequence in Central Korea: Stress Drop,
Aftershock Triggering and Fault Interaction”**

Won-Young Kim^{1,2}, Min-Seong Seo², Jun Yong Park², Sangwoo Han², Young Oh Son²,
YoungHee Kim^{2*}

¹ Lamont-Doherty Earth Observatory of Columbia University, 61 Route 9W, Palisades, NY
10964, USA

² School of Earth and Environmental Sciences, Seoul National University, 1 Gwanak-ro,
Gwanak-gu, Seoul 08826, Republic of Korea

Corresponding author: YoungHee Kim, younghkim@snu.ac.kr

Contents

This supplemental material contains additional details of the seismic data processing and analyses, as well as figures to support the main text.

Texts

- Text S1.** Waveform data for modeling and focal mechanism inversion described for the four largest events of the 2022 Goesan earthquake sequence.
- Text S2.** Corner frequency estimation.
- Text S3.** Moment magnitude estimation.
- Text S4.** Coulomb failure stress change.

Figures

- Figure S1.** Waveform data showing interferences of *P* and *S* waves from two events that occurred close in time (events 3 and 4 with 16.7 s apart).
- Figure S2.** Comparison of observed and synthetic records for the foreshock focal mechanism inversion.
- Figure S3.** Comparison of observed and synthetic records for the mainshock focal mechanism inversion.
- Figure S4.** Comparison of observed and synthetic records for focal mechanism inversion of the aftershock (event 6).
- Figure S5.** Comparison of observed and synthetic records for focal mechanism inversion of the largest aftershock (event 25).
- Figure S6.** Focal depth determination for the four earthquakes of the 2022 Goesan earthquake sequence. Calculation of observed and synthetic records for various focal depths in 1 km intervals and constraining the depth with the least fitting error.
- Figure S7.** Focal mechanisms of the five small events constrained from the *P*-wave first motion observations that are plotted as lower hemisphere projection.
- Figure S8.** Distribution of P- and T-axis of the nine earthquake focal mechanisms, the orientation of principal stress axes – σ_1 and σ_3 determined by using the stress inversion method of Gephart (1990), and the principal stress axes orientations obtained by using the method of Michael (1984).
- Figure S9.** Earthquakes located with HYPOINVERSE (map view) and with HypoDD (map view and fault plane cross-section).

Figure S10. Connectivity diagram for the double-difference earthquake relocation. Final event pair linkages for the relocation are shown. (top) A total of 1,368 correlation linkage pairs with $C_c > 0.9$. (bottom) A total of 1,020 catalog differential data linkage pairs.

Figure S11. Stacked S-wave spectral ratios and the best-fitting models for the main-EGF event pairs that are not included in Figure 5 of the main text.

Figure S12. A regression relation to estimate the moment magnitude from the local magnitude of the 2022 Goesan earthquake sequence.

Figure S13. Temporal distribution of events in the 2022 Goesan earthquake sequence.

Figure S14. Coulomb failure stress changes calculated for the foreshock with the mainshock as the receiver fault and the mainshock with three aftershocks as the receiver fault.

Text S1. Waveform data for modeling and focal mechanism inversion are described for the largest four events of the 2022 Goesan earthquake sequence.

1. ***Foreshock on 2022-10-28 at 23:27:33 (event 3):*** *P*-wave arrival times and first motion polarities are picked with clarity for stations up to about 200 km from the source. However, the *S* arrivals at stations located farther than 135 km are heavily affected by the *P* waves from the M_L 4.1 mainshock that occurred 16.7 s later. We used 3-component records from 14 stations within 60 km to model and invert them for the deviatoric-moment tensor (constrained for a double-couple mechanism). The data set includes seven accelerograms, six broadband, and single short-period records, and signals are filtered in the relatively high-frequency band between 0.3 and 1.0 Hz. The best-fit synthetics constrained the source at a 14 km depth on the two-layered crustal velocity model given by Kim and Kim (1983). The focal mechanism is predominantly strike-slip faulting on steeply dipping nodal planes (see Fig. S2). We obtained the seismic moment of $2.03 \pm 1.57 \times 10^{14}$ N m, which gives $M_W = 3.50$.
2. ***Mainshock on 2022-10-28 at 23:27:50 (event 4):*** The M_L 4.1 mainshock is the largest in the sequence and occurred 16.7 s after the M_L 3.5 foreshock. The *P*-wave arrival times and polarities are picked with confidence only for stations up to about 75 km from the source; beyond that distance, the *S* wave and its coda from the preceding M_L 3.5 event start to interfere with *P* arrivals from this shock. Hence, we limited the waveform data analysis to model and invert for the focal mechanism up to 72 km distance. The data set includes broadband, short-period, and accelerometer records from 13 stations, and signals filtered in the frequency band between 0.08 and 0.5. We obtained the seismic moment of $4.77 \pm 2.98 \times 10^{14}$ N m, which gives $M_W = 3.75$ (see Fig. S3).

3. ***Aftershock on 2022-10-28 at 23:29:18.7 (event 6)***: This shock, reported as M_L 2.9, occurred about 83.7 s after the mainshock and was preceded by a smaller event of M_L 2.2 by about 9 s. Hence, the event had limited data in the epicentral distance window of up to 45 km that could be safely analyzed without signals being interfered with the preceding event. We could model waveform data from 11 stations in a high-frequency band of 0.5–2.0 Hz. We obtained the seismic moment of $0.50 \pm 0.36 \times 10^{14}$ N m, which gives $M_W = 3.10$ (see Fig. S4).
4. ***The Largest Aftershock on 2022-10-31 at 17:27:52 (event 25)***: This shock with reported M_L 2.9 is the largest aftershock that occurred about 66 hours after the mainshock. This is the only significant event of the 2022 Goesan earthquake sequence whose records had no interference by signals from other events that occurred close in time. We modeled waveform data from 16 stations in the distance range of 8–61 km. Waveforms are modeled in a high-frequency band of 0.3–1.0 Hz. The seismic moment of $0.63 \pm 0.46 \times 10^{14}$ N m is obtained, which yields $M_W = 3.17$ (Table 2; Fig. S5).

Text S2. Corner frequency estimation

To ensure the reliability of corner frequency measurements for the five largest events (events 3, 4, 5, 6, and 25), we tested multiple main-EGF pairs for each event (except event 5). Due to low magnitudes, the number of small events that could be used as EGF event with sufficiently high SNR was severely limited. To overcome the paucity of EGF events, we tried to constrain the corner frequency by using large events as EGF events as well. Below we explain in detail the procedure corresponding to each event. We note that for events 5 and 6, only the stations up to $\Delta = \sim 50$ km could be used for spectral analysis due to significant interference by

mainshock coda at stations $\Delta > 50$ km. We also provide information about the frequency ranges selected for fitting and the number of used stations.

1) Event 3

Four main-EGF pairs ($3 - 1$, $3 - 6$, $3 - 25$, $4 - 3$) are tested. For the first three pairs, event 3 is used as the main event, while for the last pair, event 3 is used as the EGF event.

1-a) Event 3 (M_L 3.5) – Event 1 (M_L 1.6) pair (1.5 Hz – 40 Hz / N=58)

The event 1 shares similar focal mechanism with event 3, qualifying its condition to be used as EGF (Table 2, Fig. S7). The estimated corner frequencies are $f_{c1} = 8.42$ Hz and $f_{c2} = 27.38$ Hz. f_{c2} is poorly constrained due to limited bandwidth (Fig. 5a).

1-b) Event 3 (M_L 3.5) – Event 6 (M_L 2.9) pair (2 Hz – 40 Hz / N=14)

The event 6 shares similar focal mechanism with event 3, qualifying its condition to be used as EGF (Table 2). The estimated corner frequencies are $f_{c1} = 8.17$ Hz and $f_{c2} = 15.55$ Hz. Both f_{c1} and f_{c2} are visually confirmed as well constrained (Fig. S11a).

1-c) Event 3 (M_L 3.5) – Event 25 (M_L 2.9) pair (1 Hz – 40 Hz / N=59)

The event 25 shares similar focal mechanism with event 3, qualifying its condition to be used as EGF (Table 2). The estimated corner frequencies are $f_{c1} = 7.47$ Hz and $f_{c2} = 12.27$ Hz. Both f_{c1} and f_{c2} are visually confirmed as well constrained (Fig. S11b).

1-d) Event 4 (M_L 4.1) – Event 3 (M_L 3.5) pair (1 Hz – 40 Hz / N=60)

Two largest events have similar focal mechanism (Table 2) with substantial magnitude difference ($\Delta M_L = 0.6$). Thus, we can use the pair to estimate the corner frequencies of both events. The estimated corner frequencies are $f_{c1} = 5.11$ Hz and $f_{c2} = 8.27$ Hz. Both f_{c1} and f_{c2} are visually confirmed as well constrained (Fig. S11c).

By taking the average and standard deviation of values obtained with different pairs (a-d), the representative corner frequency of event 3 is given as $f_c = 8.08 \pm 0.36$ Hz.

2) Event 4

Four main-EGF pairs (4 – 1, 4 – 6, 4 – 25, 4 – 3) are tested. For all pairs, event 4 is used as the main event.

2-a) Event 4 (M_L 4.1) – Event 1 (M_L 1.6) pair (1.5 Hz – 40 Hz / N=58)

The event 1 shares similar focal mechanism with event 4, qualifying its condition to be used as EGF (Table 2, Fig. S7). The estimated corner frequencies are $f_{c1} = 5.29$ Hz and $f_{c2} = 28.78$ Hz. f_{c2} is poorly constrained due to limited bandwidth (Fig. 5b).

2-b) Event 4 (M_L 3.5) – Event 6 (M_L 2.9) pair (2 Hz – 40 Hz / N=14)

The event 6 shares similar focal mechanism with event 4, qualifying its condition to be used as EGF (Table 2). The estimated corner frequencies are $f_{c1} = 7.01$ Hz and $f_{c2} = 22.40$ Hz. However, we find that f_{c2} is poorly constrained from visual inspection (Fig. S11d).

2-c) Event 4 (M_L 4.1) – Event 25 (M_L 2.9) pair (1 Hz – 40 Hz / N=59)

The event 25 shares similar focal mechanism with event 4, qualifying its condition to be used as EGF (Table 2). The estimated corner frequencies are $f_{c1} = 4.94$ Hz and $f_{c2} = 13.73$ Hz. Both f_{c1} and f_{c2} are visually confirmed as well constrained (Fig. S11e).

2-d) Event 4 (M_L 4.1) – Event 3 (M_L 3.5) pair (1 Hz – 40 Hz / N=60)

See 1-d for the details.

By taking the average and standard deviation of values obtained with different pairs (a-d), the representative corner frequency of event 4 is given as $f_c = 5.59 \pm 0.83$ Hz.

3) Event 5

Since event 5 occurred \sim 500 m away from the main cluster, event 33 is the only qualifying EGF event. Both events share similar focal mechanisms and are nearly collocated (Figs. 3a, S11).

3-a) Event 5 (M_L 2.2) – Event 33 (M_L 1.6) pair (2 Hz – 40 Hz / N=12)

The estimated corner frequencies are $f_{c1} = 14.40$ Hz and $f_{c2} = 33.42$ Hz. f_{c2} is poorly constrained due to limited bandwidth (Fig. 5c). As only single pair is used to constrain f_c of event 5, we alternatively provide the uncertainty range by finding minimum and maximum corner frequencies such that the misfit variance does not exceed the $1.05 \times$ minimum variance (Viegas et al., 2010), which is $(f_{min}, f_{max}) = (13.35$ Hz, 15.53 Hz).

4) Event 6

Four main-EGF pairs (6 – 1, 6 – 24, 3 – 6, 4 – 6) are tested. For the first two pairs, event 6 is used as the main event, while for the last two pairs, event 6 is used as the EGF event.

4-a) Event 6 (M_L 2.9) – Event 1 (M_L 1.6) pair (1 Hz – 40 Hz / N=14)

The event 1 shares similar focal mechanism with event 6, qualifying its condition to be used as EGF (Table 2, Fig. S11). The estimated corner frequencies are $f_{c1} = 13.74$ Hz and $f_{c2} = 23.24$ Hz. f_{c2} is poorly constrained due to limited bandwidth (Fig. S11f).

4-b) Event 6 (M_L 2.9) – Event 24 (M_L 1.3) pair (2 Hz – 40 Hz / N=12)

Although focal mechanism could not be estimated due to its low magnitude, the event 24 has highly similar waveform with event 6, qualifying its condition to be used as EGF (Fig. 4c). The estimated corner frequencies are $f_{c1} = 14.46$ Hz and $f_{c2} = 30.96$ Hz. f_{c2} is poorly constrained due to limited bandwidth (Fig. 5d).

4-c) Event 3 (M_L 3.5) – Event 6 (M_L 2.9) pair (1 Hz – 40 Hz / N=14)

See 1-b for the details.

4-d) Event 4 (M_L 4.1) – Event 6 (M_L 2.9) pair (1 Hz – 40 Hz / N=14)

See 2-b for the details.

By taking the average and standard deviation of values obtained with different pairs (a-c), the representative corner frequency of event 6 is given as $f_c = 14.58 \pm 0.74$ Hz. f_{c2} estimate from the pair 4 – 6 is poorly constrained and thus excluded.

5) Event 25

Four main-EGF pairs (25 – 1, 25 – 8, 3 – 25, 4 – 25) are tested. For the first two pairs, event 25 is used as the main event, while for the last two pairs, event 25 is used as the EGF event.

5-a) Event 25 (M_L 2.9) – Event 1 (M_L 1.6) pair (2 Hz – 40 Hz / N=57)

The event 1 shares similar focal mechanism with event 25, qualifying its condition to be used as EGF (Table 2, Fig. S7). The estimated corner frequencies are $f_{c1} = 16.24$ Hz and $f_{c2} = 38.73$ Hz. f_{c2} is poorly constrained due to limited bandwidth (Fig. 5e).

5-b) Event 25 (M_L 2.9) – Event 8 (M_L 1.2) pair (3 Hz – 40 Hz / N=11)

Although focal mechanism could not be estimated due to its low magnitude, the event 8 has highly similar waveform with event 25, qualifying its condition to be used as EGF (Fig. 4c). The estimated corner frequencies are $f_{c1} = 15.57$ Hz and $f_{c2} = 48.57$ Hz. f_{c2} is poorly constrained due to limited bandwidth (Fig. S11g).

5-c) Event 3 (M_L 3.5) – Event 25 (M_L 2.9) pair (1 Hz – 40 Hz / N=59)

See 1-c for the details.

5-d) Event 4 (M_L 4.1) – Event 25 (M_L 2.9) pair (1 Hz – 40 Hz / N=57)

See 2-c for the details.

By taking the average and standard deviation of values obtained with different pairs (a-d), the representative corner frequency of event 25 is given as $f_c = 14.04 \pm 1.21$ Hz.

Text S3. Moment magnitude estimation

Seismic moments (M_0) of events 1 – 33 were estimated by fitting source model of Brune (1970) to the displacement spectrum of *S*-wave window. Waveforms recorded by broadband seismometers within 80 km of the epicenters were used in the estimation. *S*-wave windows were selected to vary between 1 – 3 s starting from manual picks on the transverse component with good signal-to-noise ratio. We removed the instrument response and integrated with respect to time in order to obtain displacement waveforms. Low-frequency plateau (Ω_0) was retrieved from best-fitting model searched by the method of Snoker (1987). We then obtained M_0 from Ω_0 using the following equation (Keilis-Borok, 1960),

$$M_0 = \frac{4\pi\rho R\beta^3\Omega_0}{F_S R_{\theta\phi}}$$

assuming *S*-wave velocity (β)=3.5 km/s, density (ρ)=2.7 g/cm³, free surface amplification factor (F_S)=2, and radiation pattern coefficient ($R_{\theta\phi}$)=0.63, with the multiplication of hypocentral distance (R) in the numerator to take geometrical spreading into account. The effect of anelastic attenuation was also considered when fitting the spectral model by using an attenuation operator, $\exp [(-\pi R f) / (\beta Q(f))]$, assuming frequency-dependent quality factor $Q(f) = 201.4f^{0.7509}$ (Kim et al., 2006). M_0 of each event was computed as a geometric mean between stations and converted to M_w .

Text S4. Coulomb failure stress change

To assess the interaction between the small earthquakes on the 2022 Goesan earthquake sequence, we calculated static Coulomb failure stress change (ΔCFS) for M_L 3.5 foreshocks and M_L 4.1 mainshock by using Coulomb 3.3 program (Toda et al., 2011). In the calculations, we set Young's modulus and Poisson's ratio as 8×10^4 MPa and 0.25, respectively. The frictional coefficient of 0.8 is used, which is within the typical range of 0.6 to 0.8 (Harris, 1998). We calculated ΔCFS for the foreshock and mainshock with several receiver faults – events 4, 6, 25, and 29. Fault geometry, focal mechanism, and other source parameters used for the main events (foreshock and mainshock) and the receiver faults are given in Table 2.

Based on ΔCFS calculation, we assess the progression of the earthquake sequence as follows:

- a) First, event 3 (M_w 3.5 foreshock) likely triggered event 4 (M_w 3.8 mainshock) about 17 s later and at ~ 0.3 km to the ESE. The Coulomb stress rose by 0.6 MPa at the mainshock location (see Fig. S10a). A few events along ESE could have been triggered by the foreshock as well.
- b) Then the mainshock triggered event 6 (M_w 3.1) about 79 s later and about 0.2 km to the northeast (Fig. S10b). This indicates the triggering of an event on the adjacent fault plane or patch, not on the same fault plane. Mainshock may have triggered three additional events close to event 6 based on the waveform similarity and their locations (see Fig. 3).
- c) Event 25 (M_w 3.2), the largest aftershock, might have been triggered about three days later by the mainshock about 0.3 km to the northwest. Coulomb stress rose by 0.2 MPa when event 25 is used as the receiver fault (see Fig. S10c).

d) Event 29 may also have been triggered by the mainshock at the location ~0.3 km SSW of the mainshock (see Fig. S14d and Fig. 3). Event 29 is within a distinct cluster A of three events (see Fig. 3c), and appears to be off the main fault plane of the sequence.

The calculations of Δ CFS suggest that the Coulomb stress increase is dominantly due to the main event fault model and focal mechanism, in particular, the fault slip direction has a dominant effect, and the location and mechanism of the receiver fault have minor effects.

Notice that the rake of the mainshock is 17° (from horizontal), which exerted stress increase at its strike direction SES – WNW as well as opposite to strike - NE – SW direction (events 6 and 29) off of the main fault.

The foreshock has nearly the same strike as the mainshock but has a rake of –19° and hence, the foreshock affects Coulomb stress increase mainly along its strike direction SES – WNW. The foreshock appears to have had very little contribution to the aftershocks that occurred opposite to the strike direction (see Fig. S14a).

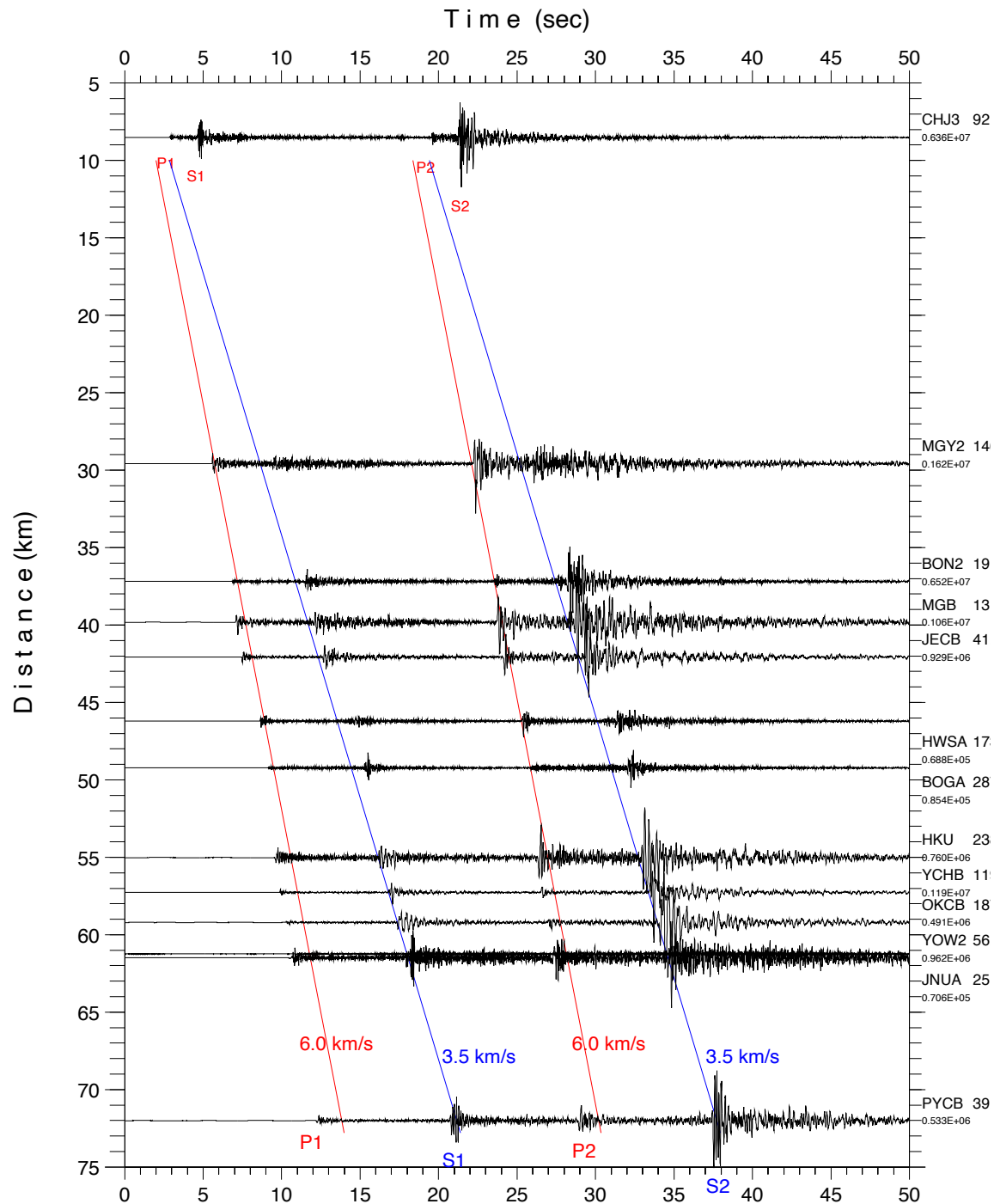


Figure S1. Vertical record section of selected stations for the foreshock (event 3 at 23:27:33.4) and the following mainshock (event 4 at 23:27:50.1). P and S waves from the two events are marked with red and blue lines, respectively, and the average speed of these waves is indicated.

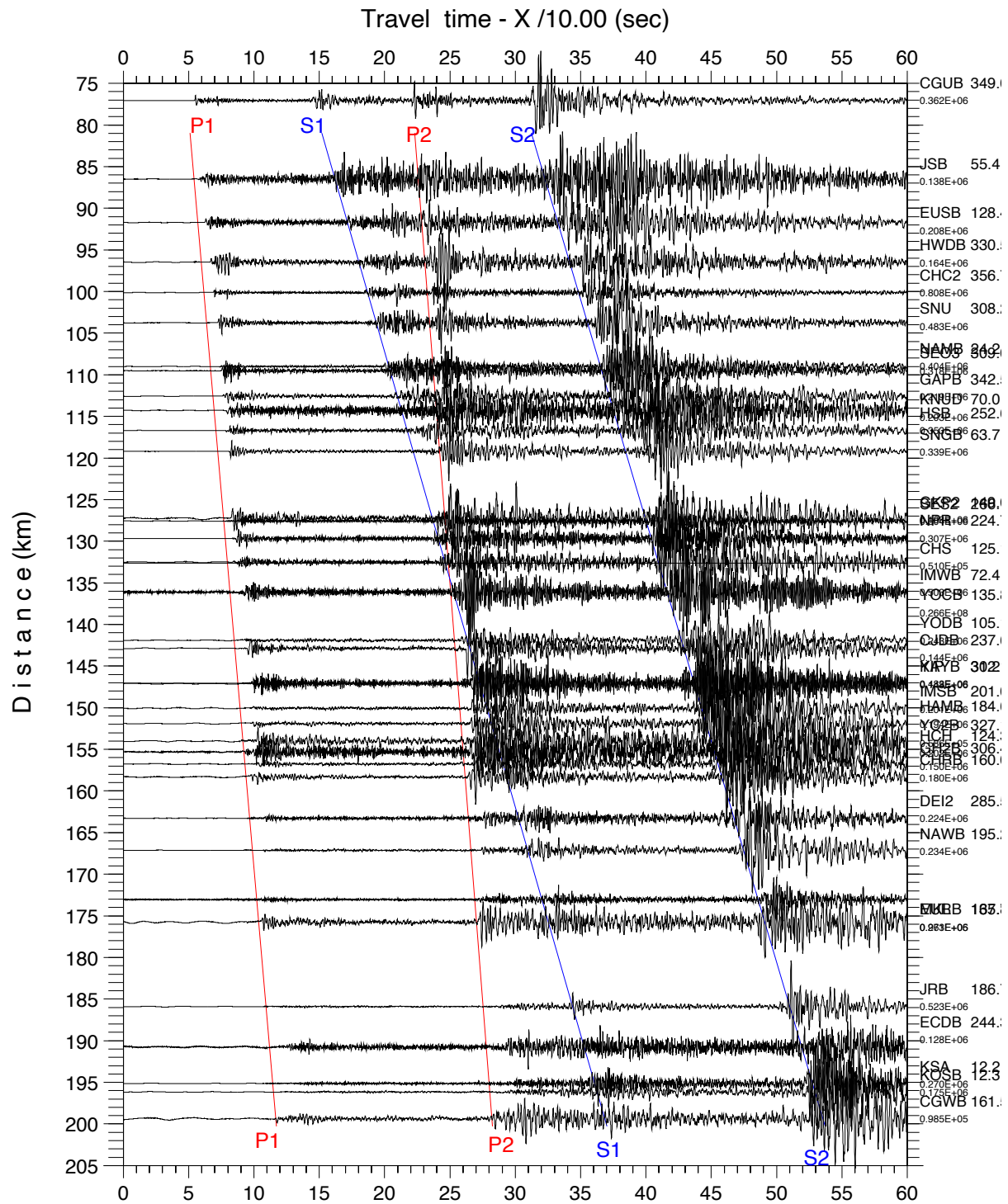


Figure S1 (Continued). Vertical records from stations at 75–200 km range. Two events are nearly collocated and occurred 16.7 s apart. Hence, *S* waves from the foreshock (S1) and *P* waves from the mainshock (P2) arrive at the same time at a distance of 135 km.

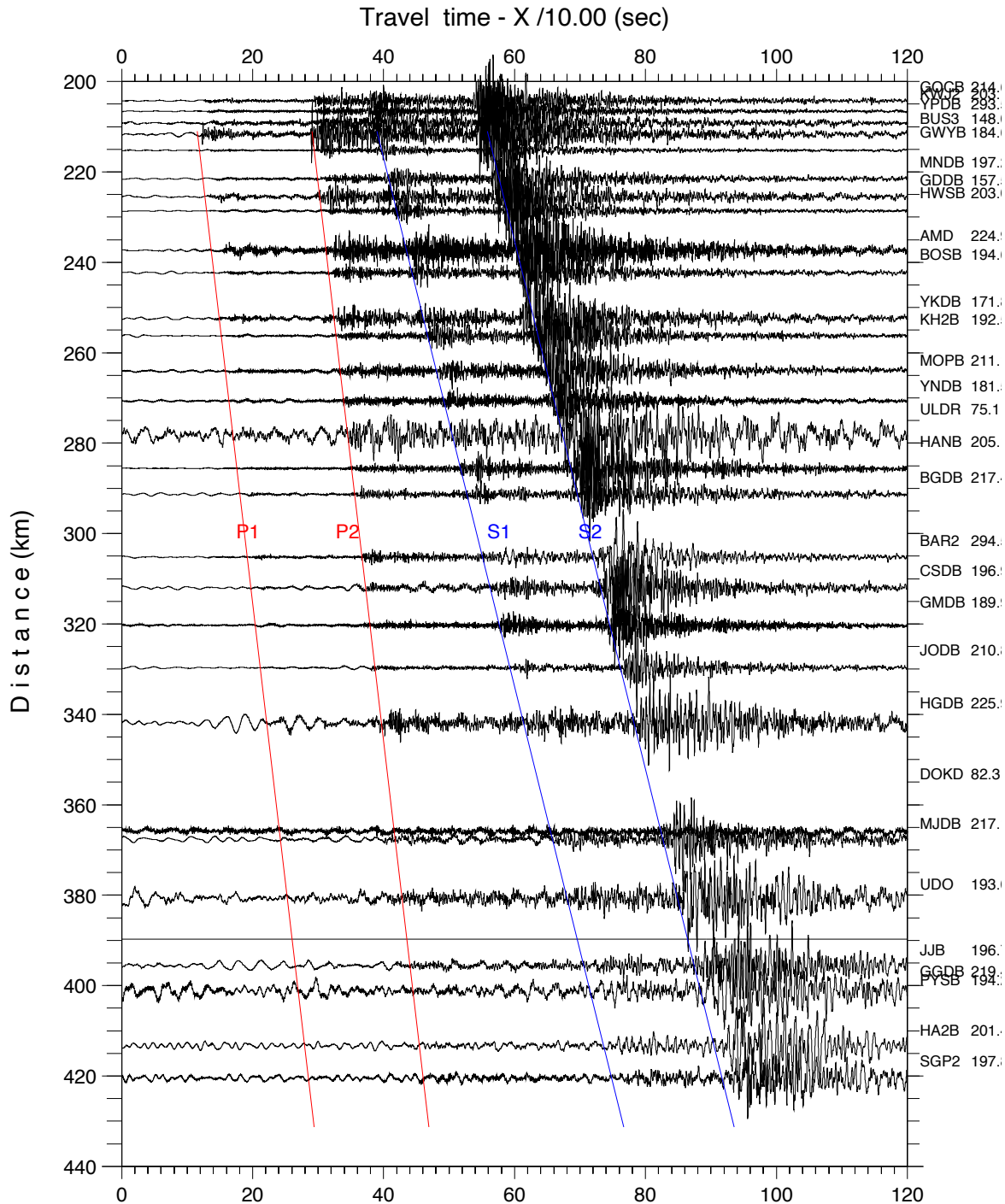


Figure S1 (Continued). Vertical records at distances 200 – 420 km. The foreshock and mainshock are nearly collocated and occurred 16.7 s apart. P2 (P waves from the mainshock) and S1(S waves from the foreshock) are hard to analyze separately and safely.

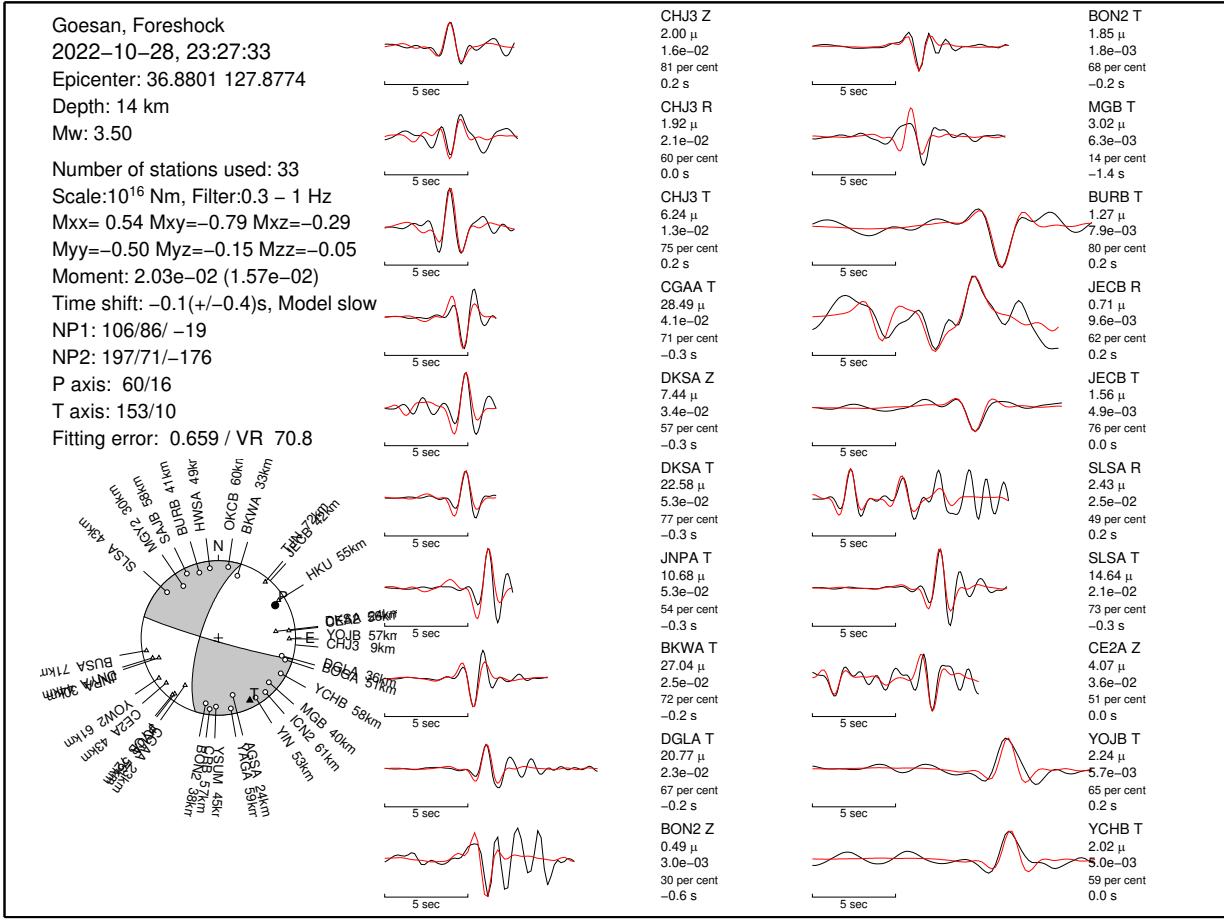


Figure S2. Comparison between observed (black lines) and synthetic (red lines) waveforms of the foreshock on 28 October 2022 at 23:27:33. Waveforms are plotted on distance range. Synthetics are calculated for a focal depth of 14 km. Station code with components (Z = vertical, R = radial, and T = transverse), peak amplitude of observed records in micrometers (μ), trace seismic moment in 10^{14} N m from the amplitude ratio between the observed and synthetics, variance reduction in percentage, and time shift in seconds are indicated at the end of each trace. The mean seismic moment is 2.03×10^{14} N m from 28 traces. The average time shift from 20 traces is -0.1 ± 0.4 s, which suggests that the synthetics are slightly slower than the observed.

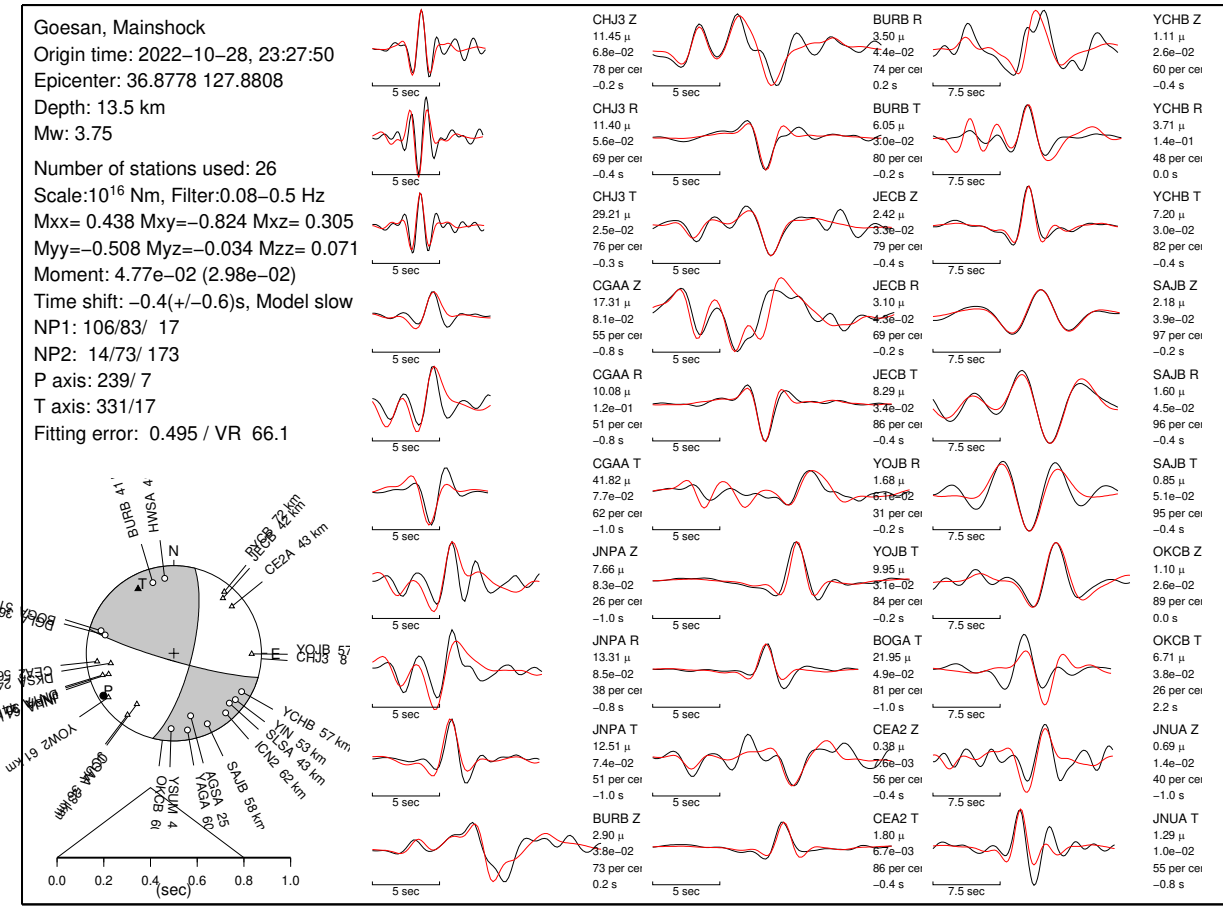


Figure S3. Comparison between observed (black lines) and synthetic (red lines) waveforms of the mainshock on 28 October 2022 at 23:27:50. Synthetics are calculated for a focal depth of 13.5 km. The mean seismic moment is 4.77×10^{14} N m from 28 traces. Other notations are the same as in Figure S2.

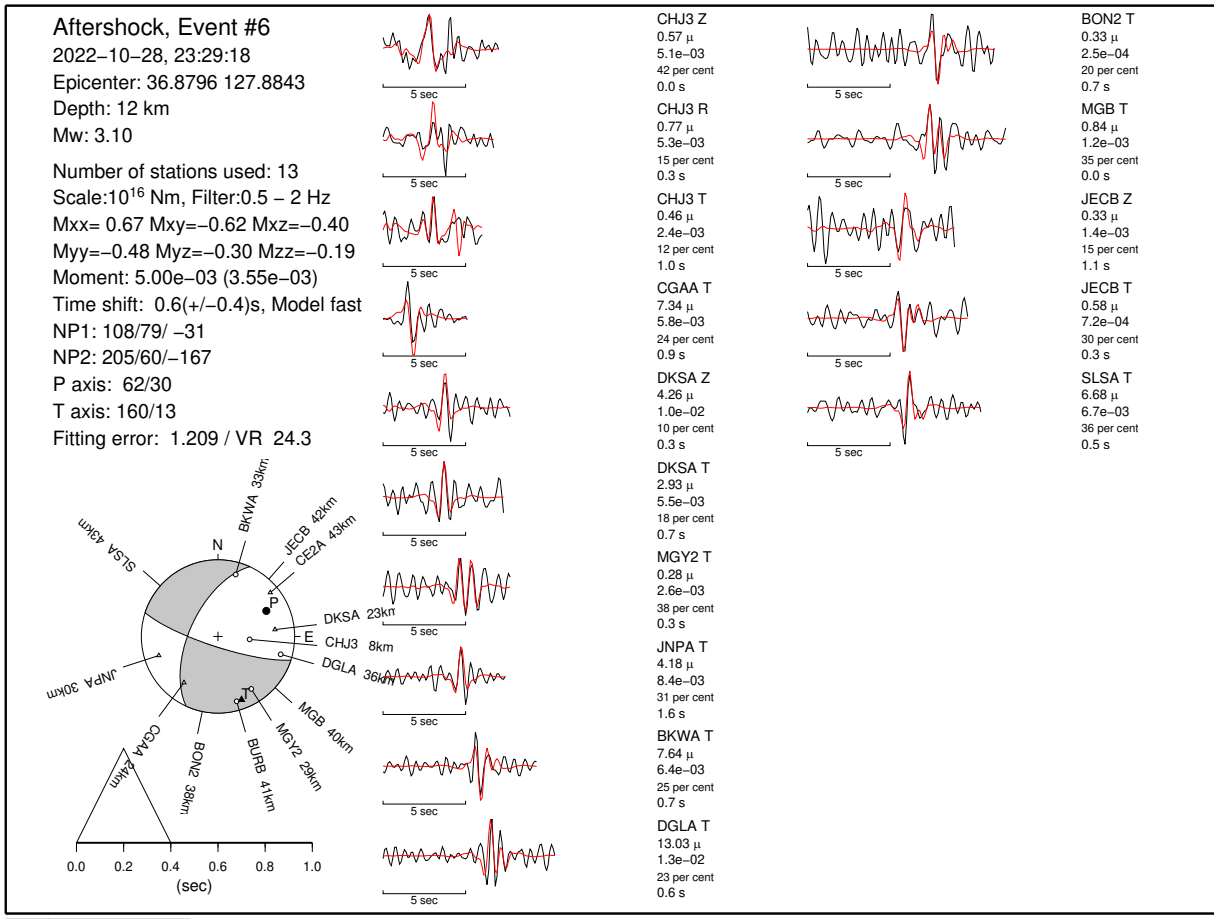


Figure S4. Comparison between observed (black lines) and synthetic (red lines) waveforms of event 6 on 28 October 2022 at 23:29:18. Synthetics are calculated for a focal depth of 12 km. The mean seismic moment is 0.50×10^{16} N m from 11 stations. Other notations are the same as in Figure S2.

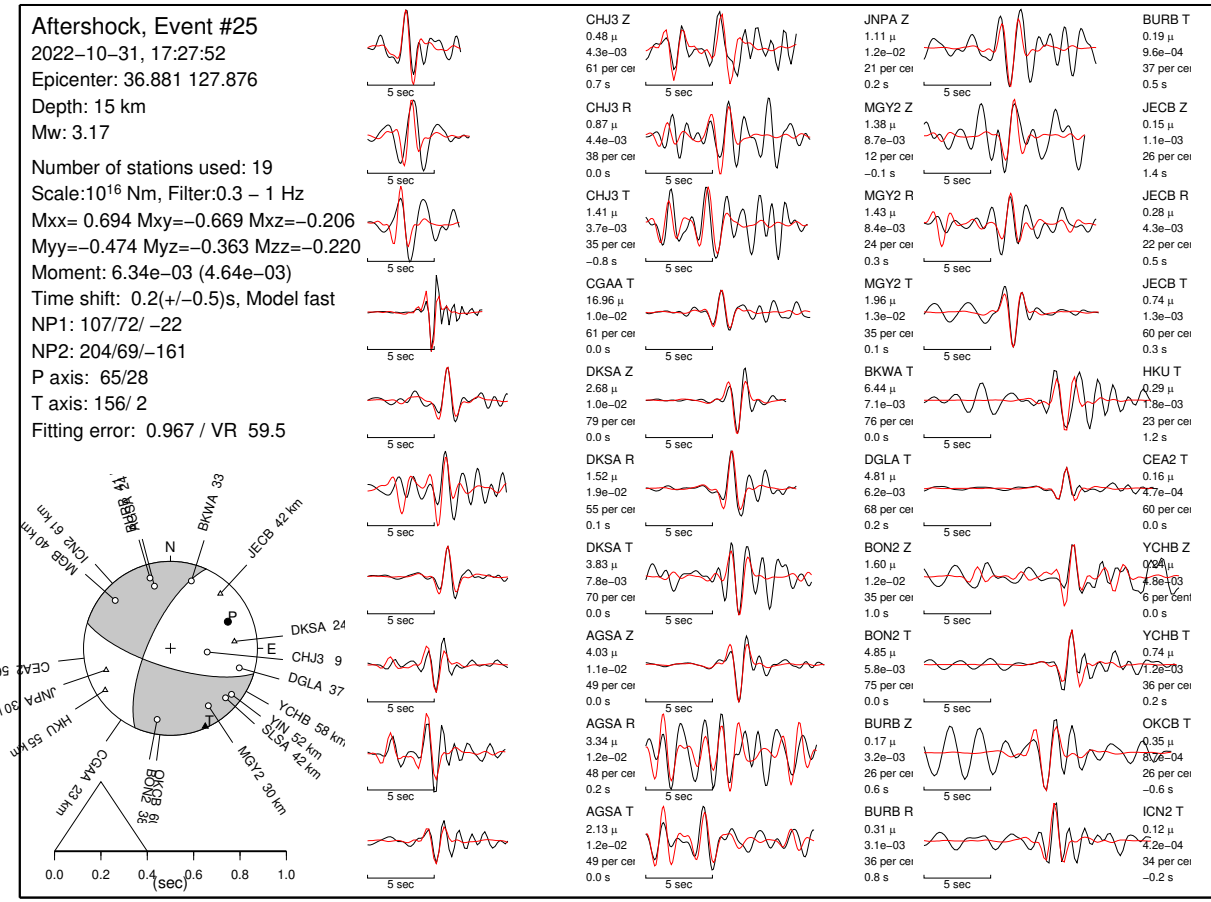


Figure S5. Comparison between observed (black lines) and synthetic (red lines) waveforms of event 25 on 31 October 2022 at 17:27:52. Synthetics are calculated for a focal depth of 15 km. The mean seismic moment is 0.63×10^{14} N m from 30 traces. Other notations are the same as in Figure S2.

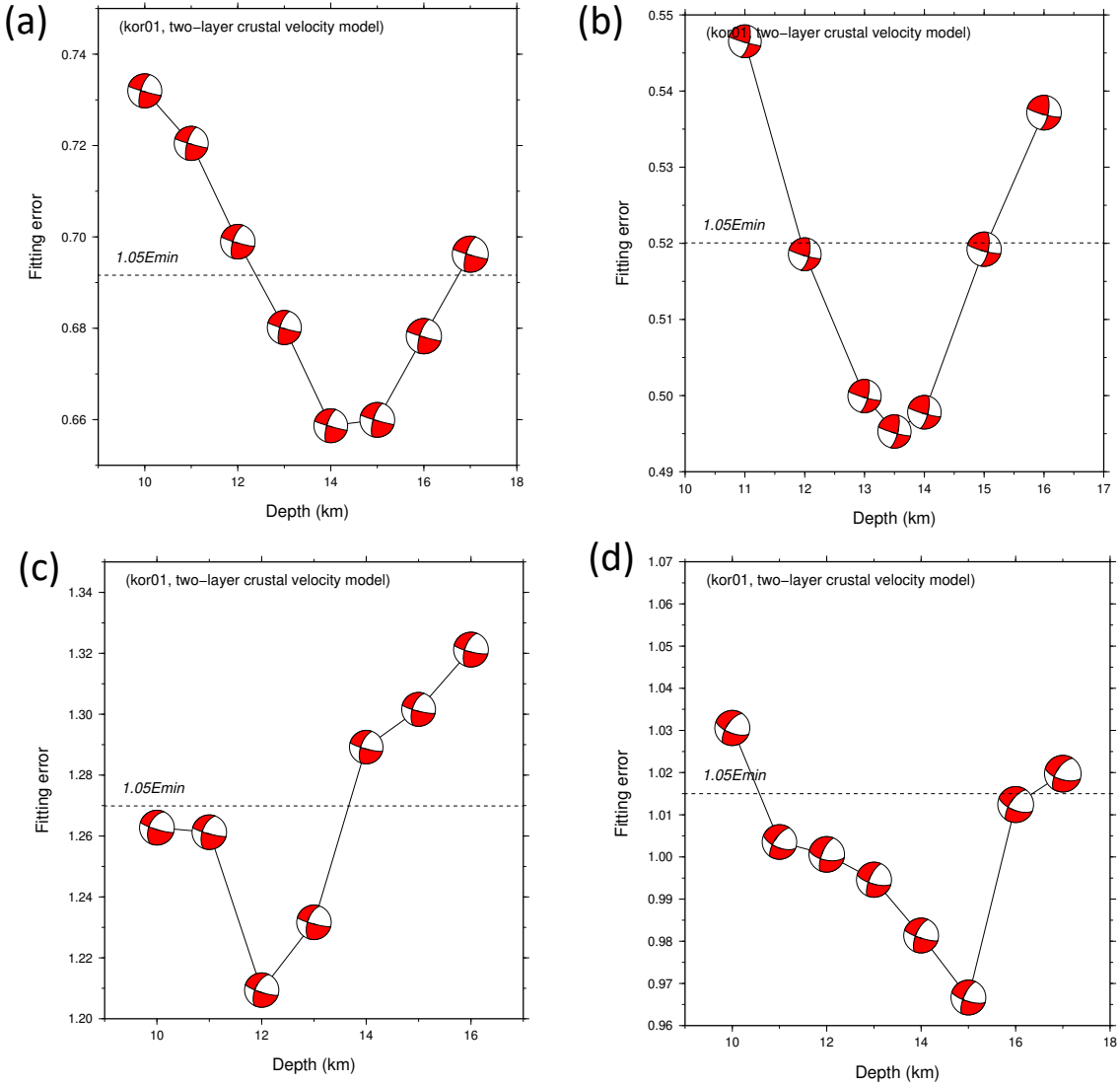


Figure S6. Changes of the fitting error (E) and source mechanism as a function of focal depth for the four earthquakes of the 2022 Goesan earthquake sequence. The fitting error reaches a global minimum (E_{\min}) at various depths. The inversion results for focal depths between 12 and 16 km produce similar overall waveform fits and source mechanisms for the four events, indicating a range of acceptable depths, and are indicated as the horizontal dashed line representing 5% greater fitting error, i.e., $1.05 \times E_{\min}$. (a) Foreshock (event 3) at 14 km, (b) mainshock (event 4) at 13.5 km, (c) aftershock (event 6) at 12 km, and (d) aftershock (event 25) at 15 km depths are constrained from these comparisons.

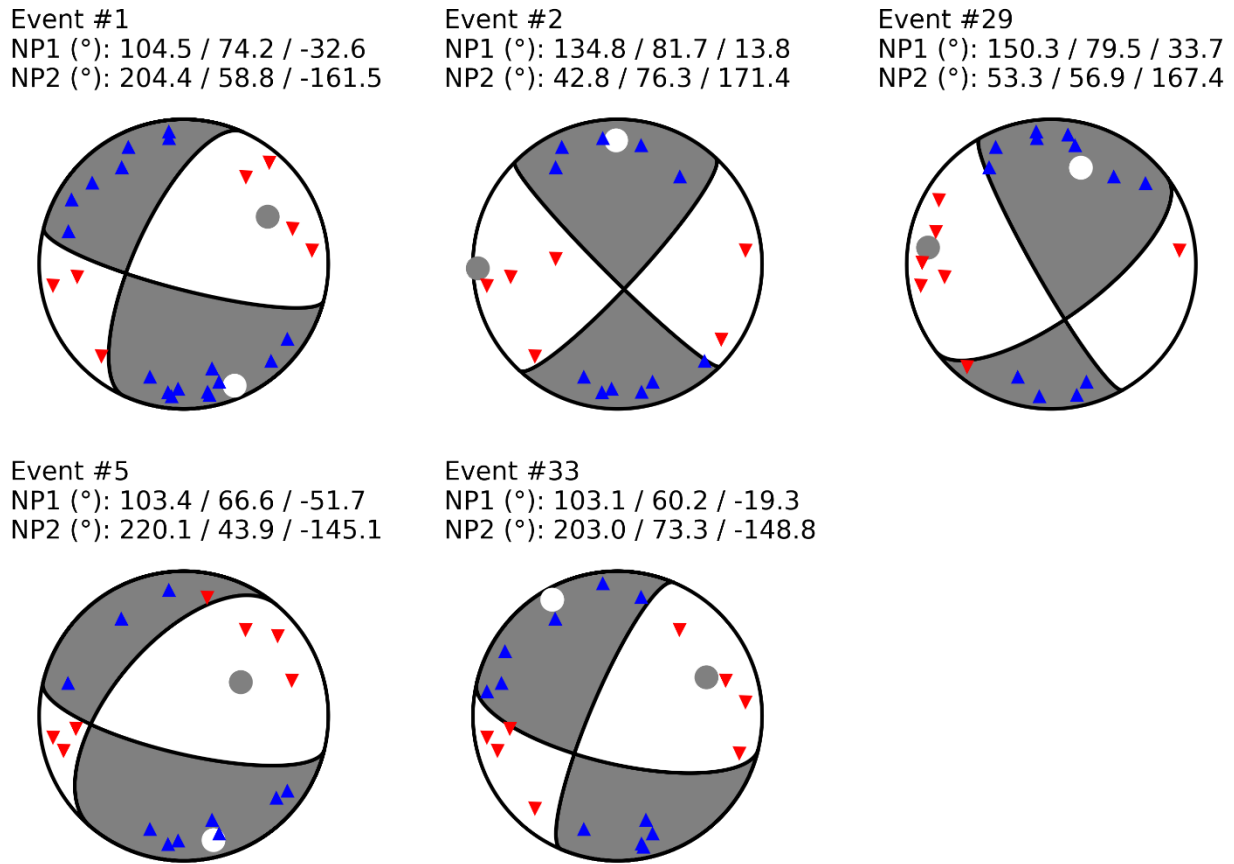


Figure S7. Focal mechanisms of the five events that are reasonably well constrained by using the P first-motion readings. These solutions are used in stress inversion. Fault plane solution of each event was obtained as the median of all possible solutions explaining the first motions of P waves using FORTRAN program, FOCMEC (Snoke, 2003). Blue triangles and red inverted triangles correspond to compressional and dilatational first motions, respectively, whereas grey and white circles indicate orientations of the P and T axes, respectively.

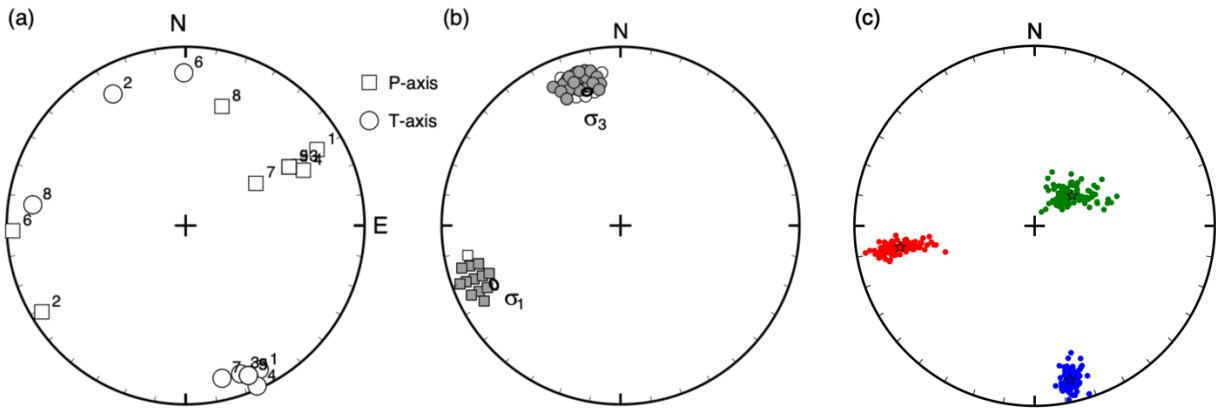


Figure S8. (a) Distribution of P axes (squares) and T axes (circles) of the nine focal mechanisms with fault plane strike direction of E-SE – W-NW used for stress tensor inversion. Each P- and T-axis is identified by the event ID number listed in Table 1. (b) Orientations of σ_1 axes (squares) and σ_3 axes (circles) of the ~40 acceptable stress models within the 95% confidence limit of the stress inversion by using the nine focal mechanisms and using FMSI (focal mechanism stress inversion) method of Gephart (1990). The best-fitting stress model (thick symbols) has an average misfit value of 2.0° and a corresponding stress ratio, R = 0.35. Symbols around the principal axes represent the dispersion in the estimates of the principal axes orientations. The orientation of σ_1 is trend 245° and plunge 19°, and σ_3 is trend 343° and plunge 22°. (c) The same data is used with the linear inversion method of Michael (1984). The uncertainty range is estimated by 100 noise realization with noise perturbations in the focal mechanisms of 5° standard deviation of the normal distribution. The red, green, and blue dots indicate the estimates of σ_1 , σ_2 , and σ_3 , respectively. The results constrained σ_1 with trend = 261°, plunge=21° (red star), and σ_3 axis with trend=167°, and plunge = 10° (blue star) with R = 0.5. If we take an arithmetic mean of two solutions, we have σ_1 ; trend=253±8° (W-SW – E-NE), plunge=20±1°, and σ_3 ; trend=345± 2° (S-SE – N-NW), plunge=6±16°. The orientation of the

stress axes is broadly consistent with an average value in the southern Korean Peninsula, but the plunge angle of the σ_1 of 20° suggests that the 2022 Goesan earthquake epicentral region may accommodate oblique faulting motion in a predominantly strike-slip regime.

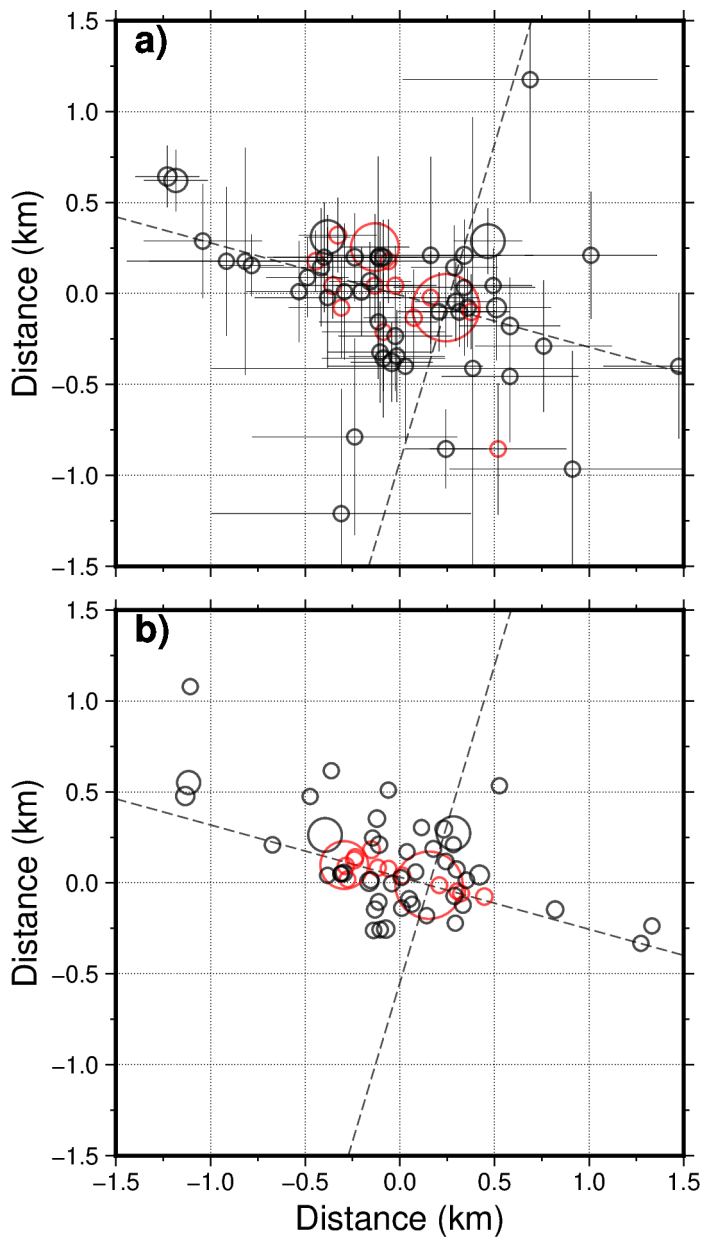


Figure S9. (a) Map-view of 63 single events (open circles) located by HYPOINVERSE with their horizontal errors at 95% confidence level. Events within the main cluster are shown in red. Dashed lines indicate nodal planes of the mainshock. (b) Map-view of relocated events using only catalog phase data. A total of 60 events are relocated using the maximum interevent separation distance of 1 km.

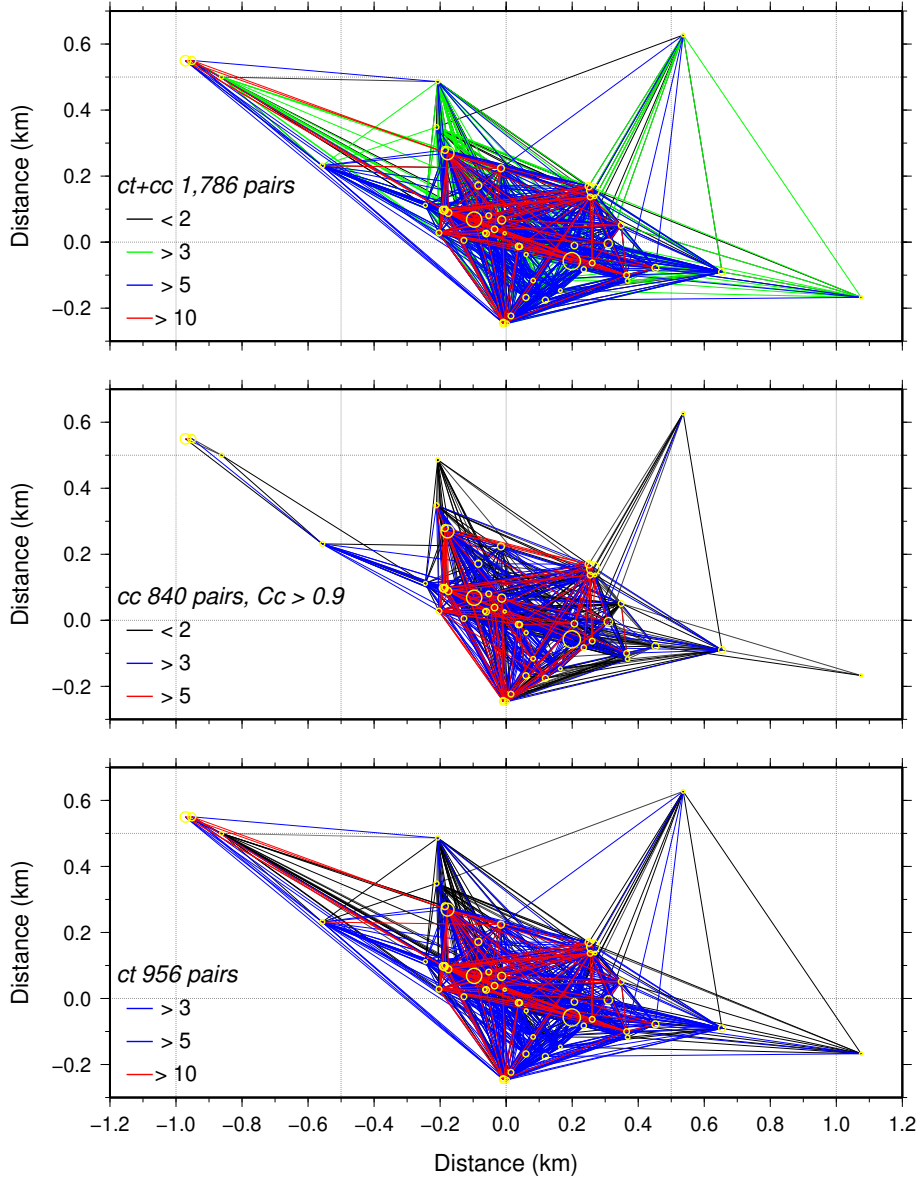


Figure S10. Connectivity diagram for the double-difference earthquake relocation. Final event pair linkages for the relocation are shown. (top) A total of 1,786 event link pairs plotted with a number of observations on each pair (color-coded). (middle) Only selected correlation data with $Cc \geq 0.9$ are used for the relocation because we have fairly good linkage and resolution from catalog data. We obtain that on average, three observations per link. Notice that events 6 (subcluster F) and 25 (subcluster I) which may form a subparallel fault plane with the mainshock plane are fairly well linked to other events to ensure reliable relocation. (bottom) 946 linkage

pairs of the catalog differential data, used for relocation. Each link has six observations on average. The mainshock has correlation link pairs with other smaller events.

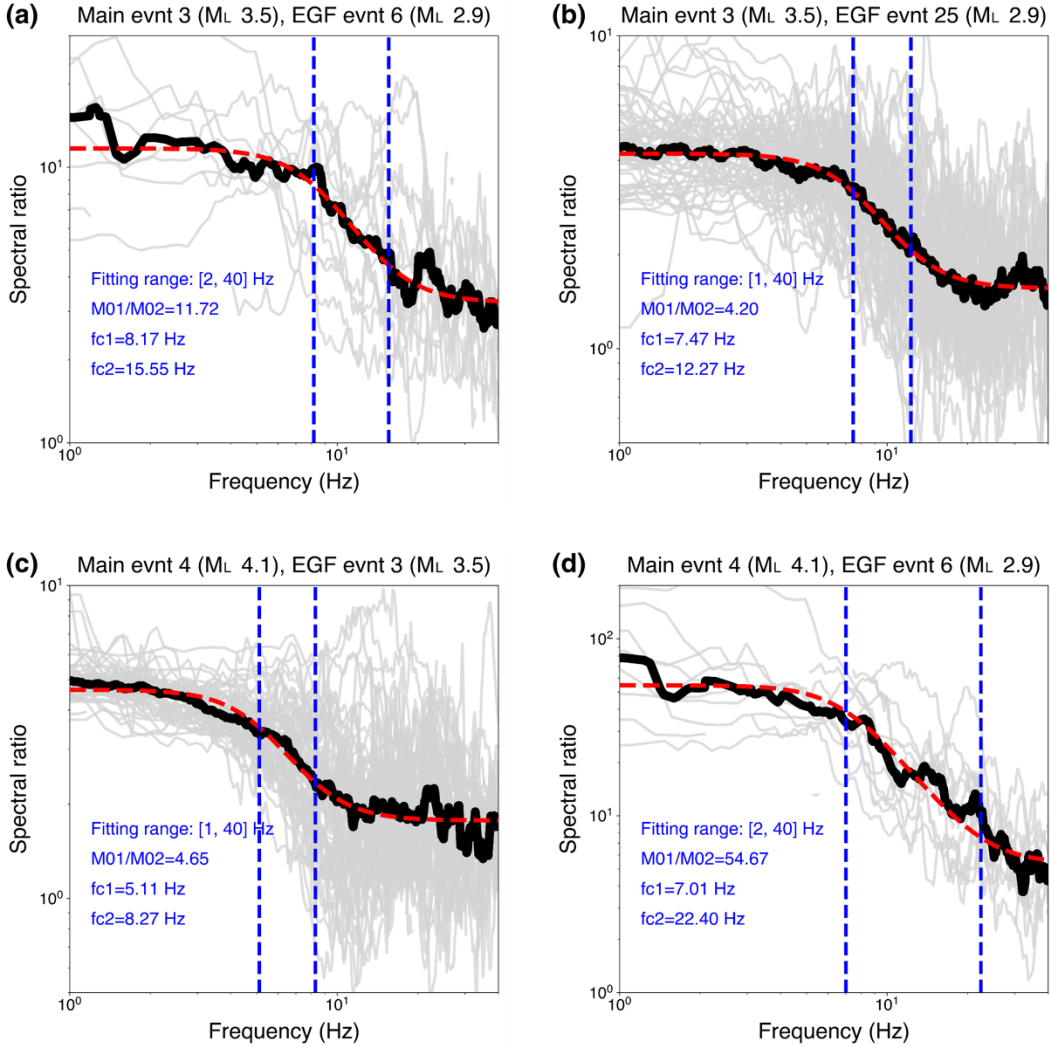


Figure S11. Stacked S-wave spectral ratios and the best-fitting models for the main-EGF event pairs that are not included in Figure 5 of the main text. (a) event 3 – 6 pair, (b) event 3 – 25 pair, (c) event 4 – 3 pair, and (d) event 4 – 6 pair. The event ID and local magnitudes of the main and EGF events are indicated atop each panel. In each panel, individual station spectral ratios are plotted as the light gray curves in the background, the stacked median spectral ratio is plotted as the thick black curve, and the best-fitting theoretical spectral ratio is plotted as the red dashed curves. Boatwright's (1980) spectral model was used for fitting. Corner frequencies f_{c1} for the main event and f_{c2} for the EGF event are denoted with the vertical blue dashed lines if they are resolved within 80 % of the Nyquist frequency (i.e., 40 Hz).

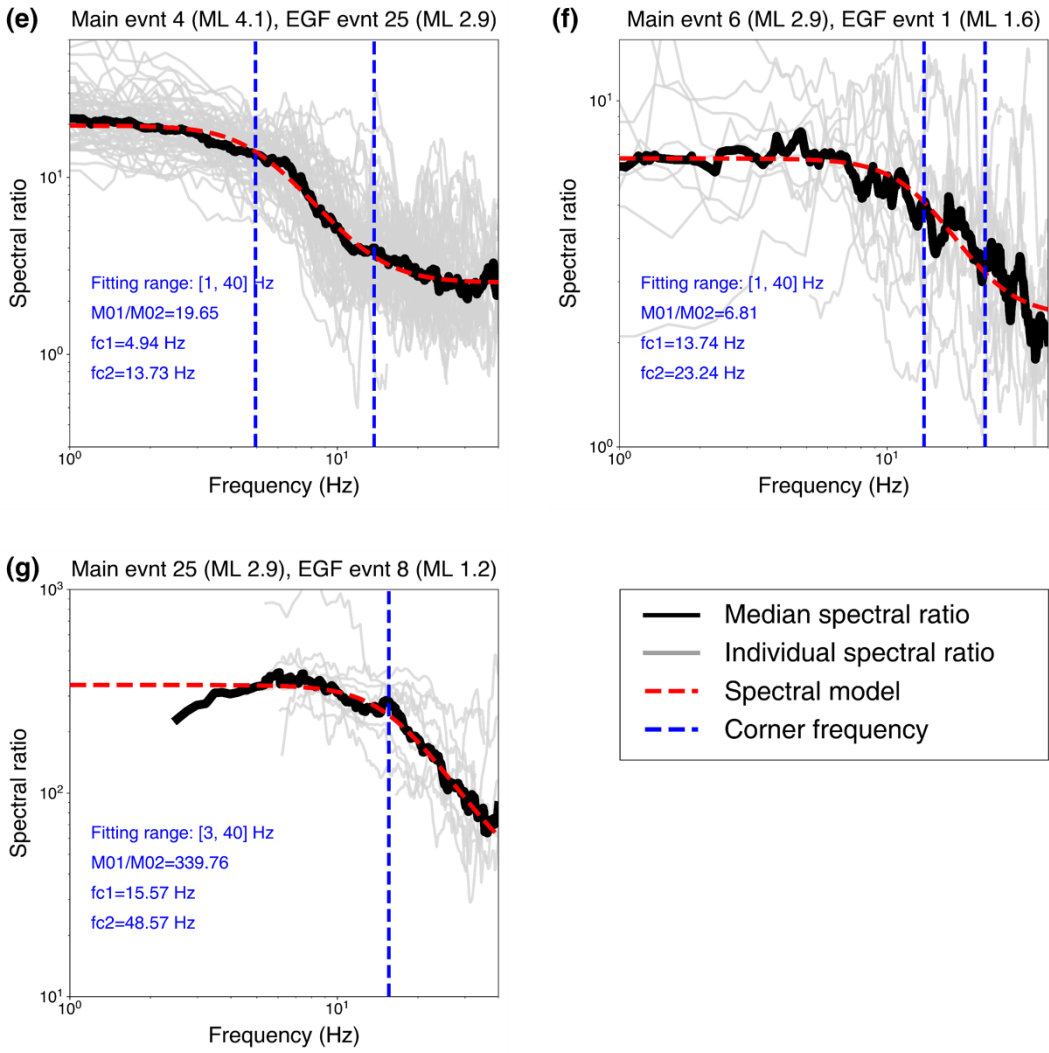


Figure S11. (Continued) Stacked *S*-wave spectral ratios the best-fitting models are shown for (e) event 4 – 25 pair, (f) event 6 – 1 pair, and (g) event 25 – 8 pair.

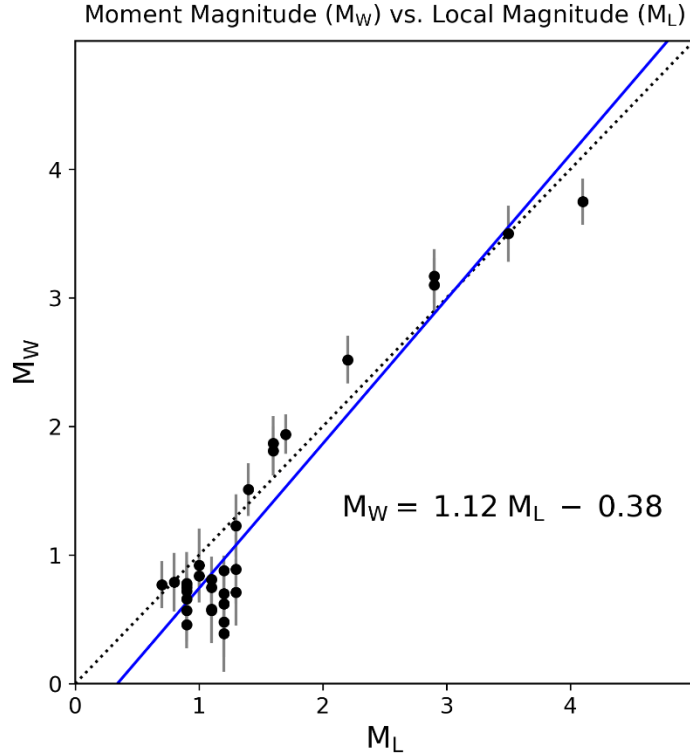


Figure S12. Comparison between M_L for 33 earthquakes from KMA catalog and corresponding M_w calculated in this study. The solid blue line is the best-fitting line obtained by weighted least-squares linear regression between M_L and M_w , whereas the black dotted line is the reference line for unity (i.e., $M_L = M_w$). Grey error bars indicate standard deviation of M_w . We obtained a linear relationship as, $M_w = 1.12 M_L - 0.38$. We calculated displacement spectrum of transverse-component data by using the multitaper approach (Prieto, 2022). We fit the omega-squared model to the observed spectrum to obtain the low-frequency level (Ω_0) via the iterative integration method (Andrews, 1986; Snoke, 1987). We obtained seismic moment (M_0) from Ω_0 assuming S -wave velocity=3.5 km/s, density=2.7 g/cm³, free surface amplification factor=2, and radiation pattern coefficient=0.63. We then calculated the event M_w from the geometric mean of M_0 for each station.

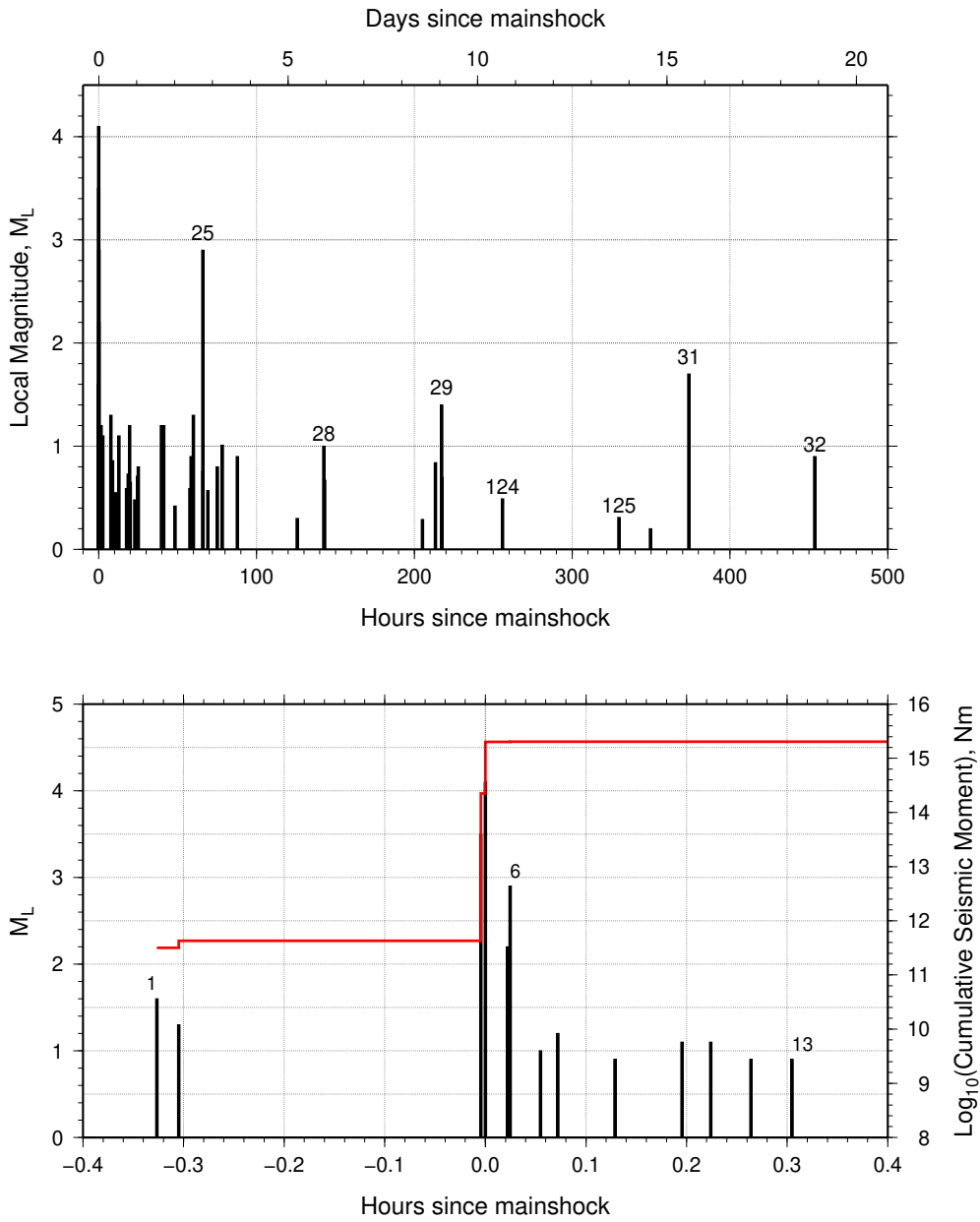


Figure S13. (top) The occurrence of 62 events of the earthquake sequence is plotted hours after the occurrence of mainshock time and against local magnitude. The last event #33 occurred on 78th day, beyond the time axis. (bottom) Detailed occurrence of the first 13 events to illustrate the nearly complete moment release during the first 0.7 hours (42 minutes) of the sequence. Cumulative seismic moment release is accomplished by the M_L 3.5 foreshock and M_L 4.1 mainshock.

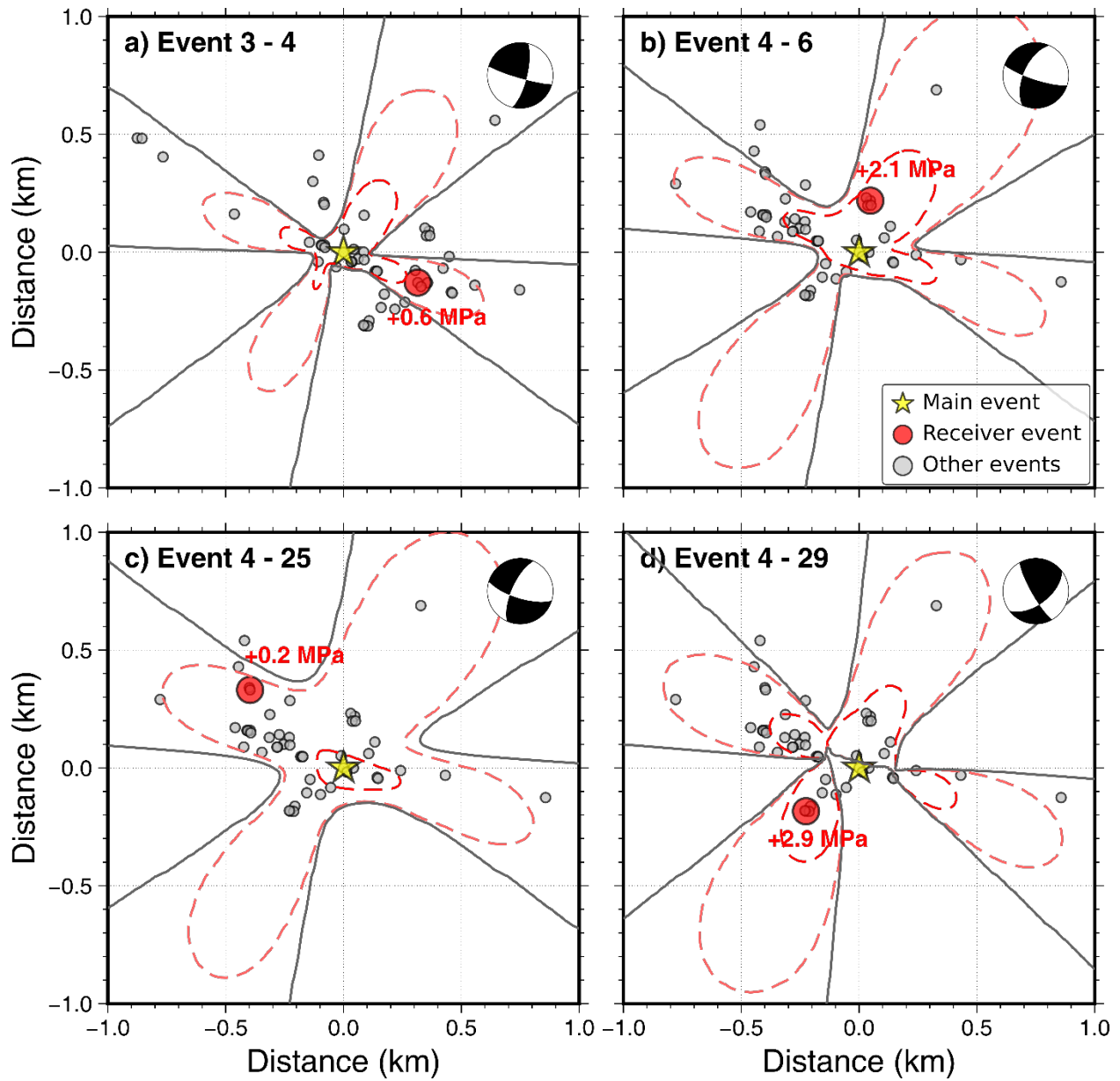


Figure S14. Map view of the Coulomb failure stress change (Δ CFS) calculated for M_L 3.5 foreshock and M_L 4.1 mainshock at receiver fault depth. In each panel, focal mechanism of the receiver event is shown as a beachball diagram, and positive stress is contoured as red dashed lines represent 1.0 and 0.1 MPa, and black solid lines represent 0.0 MPa. (a) Δ CFS for foreshock with the mainshock as receiver fault. Focal mechanism and other parameters used are given in Table 2. Coulomb stress rose by 0.6 MPa at the mainshock, and it likely triggered the mainshock,

(b) Δ CFS for the mainshock with event 6 as receiver fault. Coulomb stress rose by 2.1 MPa at the event 6 location. (c) Δ CFS for the mainshock with event 25 as receiver fault. Coulomb stress rose by 0.2 MPa at the event 25 location. (d) Δ CFS for the mainshock with event 29 as receiver fault. Coulomb stress rose by 2.9 MPa at the event 29 location.

References

- Andrews, D. J. (1986). Objective determination of source parameters and similarity of earthquakes of different size, in *Earthquake Source Mechanics*, S. Das, J. Boatwright, and C. H. Scholz (Editors), Geophysical Monograph Series, Vol. 37, American Geophysical Union, Washington, D.C., 259–267, doi: 10.1029/GM037p0259.
- Boatwright, J. (1980). A spectral theory for circular seismic sources; simple estimates of source dimension, dynamic stress drop, and radiated seismic energy, *Bull. Seismol. Soc. Am.* **70**, no. 1, 1–27.
- Brune, J. N. (1970). Tectonic stress and the spectra of seismic shear waves from earthquakes, *J. Geophys. Res.* **75**, no. 26, 4997–5009, doi: 10.1029/JB075i026p04997.
- Gephart, J. W. (1990). FMSI: A FORTRAN program for inverting fault/slikenside and earthquake focal mechanism data to obtain the regional stress tensor, *Comput. Geosci.* **16**, 953–989, doi: 10.1016/0098-3004(90)90105-3.
- Harris, R. A. (1998). Introduction to special section: Stress triggers, stress shadows, and implications for seismic hazard, *J. Geophys. Res.* **103**, no. 10, 24,347–24,358, doi: 10.1029/98JB01576.
- Keilis-Borok, V. I. (1960). Investigation of the mechanism of earthquakes, *Sov. Res. Geophys.* **4**, no. 29 (English translation).
- Kim, S. J., and S. G. Kim (1983). A study on the crustal structure of South Korea by using seismic waves, *J. Korean Inst. Mining Geol.* **16**, no. 1, 51–61.

Kim, S. K., J. Y. Yang, and J. Oh (2006). Q-values for P and S waves in the southern Korean Peninsula based on the coda-normalization method. *Geosci. J.* **10**, 465–477, doi: 10.1007/BF02910440.

Michael, A. J. (1984). Determination of stress from slip data: faults and folds, *J. Geophys. Res.* **89**, no. B13, 11,517–11,526, doi: 10.1029/JB089iB13p11517.

Prieto, G. A. (2022). Multitaper: A multitaper spectrum analysis package in Python, *Seismol. Res. Lett.* **93**, no. 3, 1922–1929, doi: 10.1785/0220210332.

Snoke, J. A. (1987). Stable determination of (Brune) stress drops, *Bull. Seismol. Soc. Am.* **77**, no. 2, 530–538.

Snoke, J. A. (2003). FOCMEC: Focal mechanism determinations, in *International Handbook of Earthquake and Engineering Seismology*, Chapter 85.12, W. H. K. Lee, H. Kanamori, P. C. Jennings, and C. Kisslinger (Editors), Academic Press, San Diego, California.

Toda, S., R. S. Stein, and J. Lin (2011). Widespread seismicity excitation throughout central Japan following the 2011 M = 9.0 Tohoku earthquake and its interpretation by Coulomb stress transfer, *Geophys. Res. Lett.* **38**, no. 7, L00G03, doi: 10.1029/2011GL047834.

Viegas, G., R. E. Abercrombie, and W.-Y. Kim (2010). The 2002 M5 Au Sable Forks, NY, earthquake sequence: Source scaling relationships and energy budget, *J. Geophys. Res.* **115**, no. B7, doi: 10.1029/2009JB006799.